



Published in final edited form as:

*Biochem Biophys Res Commun.* 2014 January 10; 443(2): 470–476. doi:10.1016/j.bbrc.2013.11.127.

## Accumulation of Nano-sized Particles in a Murine Model of Angiogenesis

Thomas Wittenborn<sup>a,\*</sup>, Esben K. U. Larsen<sup>b,c,d,\*</sup>, Thomas Nielsen<sup>a,b</sup>, Louise M. Rydtoft<sup>e</sup>, Line Hansen<sup>b,c,d</sup>, Jens V. Nygaard<sup>b,f</sup>, Thomas Vorup-Jensen<sup>d,g</sup>, Jørgen Kjems<sup>b,c,d</sup>, Michael R. Horsman<sup>a</sup>, and Niels Chr. Nielsen<sup>b,d,h</sup>

<sup>a</sup>Department of Experimental Clinical Oncology, Aarhus University Hospital, Noerrebrogade 44, 8000 Aarhus C, Denmark

<sup>b</sup>Interdisciplinary Nanoscience Center (iNANO), Aarhus University, Gustav Wieds Vej 14, 8000 Aarhus C, Denmark

<sup>c</sup>Department of Molecular Biology and Genetics, Aarhus University, C.F. Moellers Allé 3, 8000 Aarhus C, Denmark

<sup>d</sup>The Lundbeck Foundation Nanomedicine Center for Individualized Management of Tissue Damage and Regeneration (LUNA), Aarhus University, Aarhus, Denmark

<sup>e</sup>Center of Functionally Integrative Neuroscience (CFIN), Aarhus University Hospital, Noerrebrogade 44, 8000 Aarhus C, Denmark

<sup>f</sup>Department of Engineering, Aarhus University, Finlandsgade 22, 8000 Aarhus, Denmark

<sup>g</sup>Department of Biomedicine, Aarhus University, Bartholins Allé 6, 8000 Aarhus, Denmark

<sup>h</sup>Center for Insoluble Protein Structures (inSPIN) and Department of Chemistry, Aarhus University, Gustav Wieds Vej 14, 8000 Aarhus C, Denmark

### Abstract

**Purpose**—To evaluate the ability of nm-scaled iron oxide particles conjugated with Azure A, a classic histological dye, to accumulate in areas of angiogenesis in a recently developed murine angiogenesis model.

**Materials and Methods**—We characterized the Azure A particles with regard to their hydrodynamic size, zeta potential, and blood circulation half-life. The particles were then investigated by Magnetic Resonance Imaging (MRI) in a recently developed murine angiogenesis model along with reference particles (Ferumoxtran-10) and saline injections.

© 2013 Elsevier Inc. All rights reserved.

**CORRESPONDING AUTHOR:** Thomas Rea Wittenborn. Department of Experimental Clinical Oncology, Aarhus University Hospital, Nørrebrogade 44, Building 5, 2nd floor. DK-8000 Aarhus C, Denmark. Telephone: + 45 78462627, Wittenborn@oncology.dk.

\*First and second author contributed equally to the manuscript.

**Publisher's Disclaimer:** This is a PDF file of an unedited manuscript that has been accepted for publication. As a service to our customers we are providing this early version of the manuscript. The manuscript will undergo copyediting, typesetting, and review of the resulting proof before it is published in its final citable form. Please note that during the production process errors may be discovered which could affect the content, and all legal disclaimers that apply to the journal pertain.

### DISCLOSURES

None

### ETHICS

All procedures involving animal experiments were approved by the National Animal Experiments Inspectorate.

**Results**—The Azure A particles had a mean hydrodynamic diameter of  $51.8 \pm 43.2$  nm, a zeta potential of  $-17.2 \pm 2.8$  mV, and a blood circulation half-life of  $127.8 \pm 74.7$  minutes. Comparison of MR images taken pre- and 24-hours post- injection revealed a significant increase in  $R_2^*$  relaxation rates for both Azure A and Ferumoxtran-10 particles. No significant difference was found for the saline injections. The relative increase was calculated for the three groups, and showed a significant difference between the saline group and the Azure A group, and between the saline group and the Ferumoxtran-10 group. However, no significant difference was found between the two particle groups.

**Conclusion**—Ultrahigh-field MRI revealed localization of both types of iron oxide particles to areas of neovasculature. However, the Azure A particles did not show any enhanced accumulation relative to Ferumoxtran-10, suggesting the accumulation in both cases to be passive.

## Keywords

Angiogenesis; iron oxide particles; ultrahigh-field MRI; sponge model

## INTRODUCTION

Angiogenesis has been established as a common feature of many pathological conditions including diseases such as atherosclerosis and cancer [1, 2]. During the angiogenetic process and in the initial phase of neovascular maturation, the vessels tend to be fragile and leaky because of a discontinuous or missing basal membrane [3, 4]. These leaky vessels introduce a potential route of transport from the blood into the extravascular extracellular space (EES) and extracellular matrix (ECM) [5, 6, 7]. The ECM contains an abundance of heavily glycosylated proteins, in particular sulphated glucosaminoglycans [8], which under physiological conditions are negatively charged.

These combined features can be exploited for drug delivery or imaging [5, 6, 7, 9], and has made angiogenesis a desired target for new nanotechnological approaches. The field of nanotechnology has expanded markedly within the past decades and has now developed to such an extent that it has become possible to manufacture tailor-made nm-scaled particles to target specific biomarkers of biological processes [10, 11, 12, 13, 14, 15].

Azure A, a small positively charged metachromatic dye used for decades in histology [16], has been known to stain DNA, azurophilic granules of leukocytes, and other negatively charged molecules [17, 18, 19, 20]. By conjugating this small dye to a nano-sized particle it could enable binding of the particle to the negatively charged proteoglycans in the ECM.

Here, we describe the physicochemical characterization and accumulation properties of such an Azure A-conjugated iron oxide nano-sized particle. Hydrodynamic size, zeta potential, and blood circulation half-life were estimated using standard methods, and its ability to localize to areas of angiogenesis was assessed by ultrahigh-field MRI in a recently described murine angiogenesis model [21].

## MATERIALS AND METHODS

### Materials

Diethyl ether, 3-Amino-7-(dimethylamino)-phenothiazin-5-ium (Azure A) and (3-Aminopropyl)-triethoxysilane (Si-NH<sub>2</sub>) were purchased from Sigma-Aldrich, St Louis, MO, USA. NHS-PEG-Maleimide (PEG molecular weight of 2000 Da) was purchased from IRIS biotech GmbH, Marktredwitz, Germany. Methoxy PEG succinimidyl active ester (NHSPEG; PEG molecular weight of 2000 Da) was purchased from Rapp-polymere GmbH.

## Synthesis of Azure A conjugated nano-sized particles

The synthesis of oleic acid-coated iron oxide particles is described by Larsen et al. [7]. Iron oxide particles (50 mg) coated with oleic acid were dissolved in 5 mL toluene. Under constant stirring, 10  $\mu$ L Si-NH<sub>2</sub> (55.8  $\mu$ mol), 38 mg NHS-PEG (50.7  $\mu$ mol), 0.8 mL triethylamine (TEA) and 80  $\mu$ L H<sub>2</sub>O were added. After overnight reaction particles were heated to 105°C for 1 hour and washed in toluene/pentane three times. To conjugate Azure A, 15 mg particles were first conjugated to 90 mg NHS-PEG-Maleimide (45  $\mu$ mol) and reacted together with 90  $\mu$ L DIC (714  $\mu$ mol) and 200  $\mu$ L TEA in toluene for 24 hours. Particles were washed in toluene/pentane three times. Then 9 mg Azure A was added to the particle formulations in 1 mL DMSO with 60  $\mu$ L TEA for 24 hours. Finally, the particles were precipitated with diethyl ether. Particles were purified by dialysis (6–8 kDa cut-off) against PBS for 5 days, changing the solute twice a day. Following dialysis the particles were centrifuged to remove aggregates.

## Characterization of functionalized particles

The hydrodynamic size and zeta potential of the Azure A particles were assessed by dynamic light scattering (DLS) using a Zetasizer Nano ZS (Malvern Instruments, Malvern, UK). Measurements were made in phosphate buffered solution at pH 7.0 and 25 °C. Three consecutive measurements were performed and the mean  $\pm$ standard deviation was calculated.

To determine blood circulation half-life, particles were diluted in saline and injected intravenously (i.v.) into male CDF1 mice. Three mice were injected with the Azure A particle formulation and six mice were injected with the Ferumoxtran-10 formulation. A volume of 10  $\mu$ L/g of mouse body weight was administered at a dose of 5 mg Fe/kg. A control group with three mice received i.v. saline injections also in a volume of 10  $\mu$ L/g. Blood samples were drawn from the suborbital sinus of animals prior to injection and 5, 60, 360 and 1440 minutes after injection. Blood was collected in EDTA tubes, and blood samples were centrifuged to obtain EDTA-plasma. Samples were digested using a solution of 5.5 mL Nitric acid (HNO<sub>3</sub>) and 0.5 mL Hydrochloric acid (HCl, 12M), which was heated to speed up the process. Iron concentrations in the samples were analysed by inductively coupled plasma atomic emission spectroscopy (ICP-AES) using a Plasma 2000 (Perkin-Elmer, USA) as described elsewhere [22]. Blood circulation half-life was calculated based on linear regression of the exponential washout of the injected particles.

## Angiogenesis model

Fifteen male CDF1/Tac mice (12–20 weeks old) were included in the experiment. Polycaprolactone (PCL) discs were made in-house and prepared according to Andersen et al. [23]. The procedure for implantation of porous PCL discs has been previously described [21]. In brief, a small incision (1.5 cm) was made in the skin on the back, through which the PCL discs (measuring 8mm in diameter and 2-3mm in height) were subcutaneously implanted. After surgery the mice were caged individually for 3–4 weeks, which was the optimal time point after implantation for a maximum amount of neovessels [21]. Mice were distributed equally into three groups: a saline group, a reference group (Ferumoxtran-10), and an Azure A-conjugated group (Azure A).

## MRI of injected particles

A 16.4 T spectroscopy/imaging system (wide-bore Bruker 700 Avance-II, Bruker Biospin, Rheinstetten, Germany) equipped with a GREAT 60 gradient system with a maximum gradient strength of 1.5T/m and a Micro 2.5 probe (coil inner diameter 25mm) was used for the in vivo MRI. Mice were anaesthetized by intraperitoneal (i.p.) injection (10  $\mu$ L/g of a

mixture of 10mg/mL ketamine and 1mg/mL xylazin) and supplemented with top-up doses (5  $\mu\text{L/g}$ ) when needed. An i.p. line was connected to a syringe primed with anaesthesia to administer top-up doses. A respiration-monitoring pad was attached to the abdomen of the mice using tape and connected to a monitoring system. Mice were placed with the tissue of interest aligned to the middle of the coil. Mice were restrained using tape and the entire setup was inserted into the vertical MR scanner. Here mice were kept warm by a circulating water system around the gradients (30 °C). A pre-scan was performed and after that particles were diluted in saline and administered i.v. at a dose of 2.5 mg Fe/kg (resembling a concentration of 0.25  $\mu\text{g}/\mu\text{L}$  injected at 10  $\mu\text{L/g}$ ). In the saline group, saline was administered in equal amounts (10  $\mu\text{L/g}$ ), and 24 hours post-injection all mice were scanned again (24 hours post-scan).

$R_2$  and  $R_2^*$  measurements were performed before and 24 hours after administration of the particles using gradient echo and spin echo sequences. The measurements were performed on 10 transverse slices of 0.5 mm thickness and 0.5 mm spacing. For both gradient echo and spin echo experiments additional scanning parameters were:  $T_R = 4000$  ms, field of view = 25×25 mm, acquisition matrix 256×192 reconstructed to 256×256, acquisition matrix 256×128 reconstructed to 256×256, or acquisition matrix 128×96 reconstructed to 128×128, and number of averages = 1. In the gradient echo sequence, the flip angle was 90°, and 12  $T_E$  within the interval 3.4 to 58.4 ms were used, and in the spin echo sequence, 12  $T_E$  values within the interval 8.1 to 117.3 ms were used. Data analysis was performed using MATLAB 7.11 (The MathWorks, Inc., Natick, MA, USA).  $R_2$  and  $R_2^*$  maps were produced by nonlinear least squares fitting of the image signal  $S$  for different echo times ( $T_E$ s) to the equation  $S(T_E) = S(0)\exp(-T_E \cdot R_2^*)$ . Regions of interest (ROIs) were drawn manually on a raw image to contain the entire implanted scaffolds. From the characterization of the angiogenesis model [21] we learned that the vasculature covered most, but not all, of the implant after 3-4 weeks. To avoid nonvascularized areas in our analysis we did the following: for the pre-scan ROIs, voxels with  $R_2 < 25 \text{ s}^{-1}$  and  $R_2^* < 95 \text{ s}^{-1}$  were removed for  $R_2$  and  $R_2^*$  analysis, respectively. These values were based on the bimodal shape of the pooled ROI histograms for all the animals (Figure 1). Because the mice were repositioned before the 24 hours post-scan, and new ROIs were drawn, we assumed that the same ROI percentage was vascularised at this time point. From the post-scan ROIs we then excluded the lowest  $R_2$  or  $R_2^*$  values leaving the same ROI voxel percentage as in the pre-scan for analysis.

Some of the obtained images suffered from water-fat shift, susceptibility or motion artefacts, resulting in poor image quality and overestimated relaxation rates. In some spin-echo images the water-fat-shift was problematic. These artefacts/anomalies discredited the obtained values from the maps. Hence, images were sorted in the following way: 1) Images including no or only extreme peripheral regions of the implants were excluded. 2) Images containing unnatural values for some regions in muscle tissue or bladder content were excluded; we would expect these tissues to have the same value throughout the entire structure, as their composition is uniform. The images that were left had ROIs drawn around the implants and were used in the quantitative analysis.

### Statistical analysis

Data are presented as mean ( $\pm$ standard deviation) of individual ROI means. Comparison of relaxation rates before and after injection of the particles was evaluated using Student's T-test ( $R_2$  and  $R_2^*$ ). Comparison of the relative increase between the different groups was made by one-way analysis of variance (ANOVA) followed by Student's Newman-Keuls multiple comparison test using SigmaPlot version 11.0. A value of  $P < 0.05$  was considered significant.

All procedures involving animal experiments were approved by the National Animal Experiments Inspectorate.

## RESULTS

Characterization of the Azure A particle revealed a hydrodynamic size of  $51.8 \text{ nm} \pm 43.2 \text{ nm}$ , a zeta potential of  $-17.2 \text{ mV} \pm 2.8 \text{ mV}$ , and a blood circulation half-life of  $127.8 \text{ min.} \pm 74.7 \text{ min.}$  As comparison, Ferumoxtran-10, which has been described by Casula et al. [24], had a hydrodynamic size of  $34 \text{ nm}$ , and a zeta potential of  $-12.6 \text{ mV} \pm 1.8 \text{ mV}$ . Blood circulation half-life was not investigated by Casula et al., but we found this to be  $131.2 \text{ min.} \pm 7.1 \text{ min.}$

Both particles were evaluated for angiogenesis localization in the murine model by an ultra-high-field 16.4T spectroscopy/imaging system, and compared to saline injections. Pre- and 24 hours post-injection  $R_2$  and  $R_2^*$  maps were generated from the recorded MR-images, and regions of interest (ROIs) were drawn around the implanted scaffolds and overlaid on the raw images. A minimum threshold value was set on the pre-injection  $R_2$  and  $R_2^*$  maps to exclude non-vascularized areas within the implants, and the same percentage amount of voxels were excluded from their post-injection  $R_2$  and  $R_2^*$  map counterparts (Figure 2). Remaining areas were then used to calculate mean relaxation rates of  $R_2$  and  $R_2^*$  before and after injection of the particles (Figure 3).  $R_2^*$  relaxation rates showed significant increase for both the Azure A particle and the Ferumoxtran-10 particle compared to pre injection. The mean  $R_2$  relaxation rates showed a higher but nonsignificant increase for both particles. The relative increase was calculated for both  $R_2$  and  $R_2^*$  relaxation rates (Figure 4) where  $R_2^*$  relaxation rates revealed a significant increase of both the Azure A and Ferumoxtran-10 group compared to saline. When analysing the  $R_2$  relaxation rates both particle groups had a higher but non-significant increase compared to saline.

## DISCUSSION

Characterizing novel particles require assessment of both physicochemical and biological properties. Size, surface charge and blood circulation half-life are parameters that need to be addressed in order to give a proper evaluation of a novel particle. Particles with hydrodynamic diameters below 20–30 nm are prone to quicker excretion through the kidneys, whereas particles with a hydrodynamic diameter above 150 nm are prone to faster clearance by the reticuloendothelial system through the phagocytic uptake in liver and spleen [25, 26, 27]. Insufficient coating of particles with polyethylene glycol (PEG) can result in a high-numerical zeta potential leading to faster clearance by the reticuloendothelial system, but with a sufficiently thick coating layer the zeta potential becomes more neutral leading to less uptake of particles [28]. A long blood circulation half-life should permit sufficient time for particles to extravasate and accumulate in the areas of interest provided that the blood flow to the tissues are not compromised [10].

We attached a PEG coating to an iron oxide core in order to shield the particle from being cleared by the reticuloendothelial system. Azure A was conjugated to this particle to create a potential ECM-targeting moiety. Assessment of size, surface charge and blood circulation half-life for the Azure A particle and comparison with the well described Ferumoxtran-10, showed several similarities and indicated that the Azure A particle was not readily removed from the blood stream (blood circulation half-life of  $127.8 \text{ min.} \pm 74.7 \text{ min.}$ ).

Choosing the right model for evaluating targeting potential of novel particles is very important. Tumour-associated angiogenesis models have predominantly been used to evaluate angiogenesis-targeted nanoprobes [13, 29, 30, 31, 32, 33, 34]. This is probably due

to the extreme amount of neovessels in tumours or because cancer-treatment/diagnosis is the endpoint for the nanoprobe in question. However, the universal disease-treatment potential of these probes remain unclear as tumour-associated angiogenesis is influenced to a great extent by tumour-cells expressing extreme amounts of pro-angiogenic factors. In other words, functionalized nanoparticles identifying or targeting tumour angiogenesis will not necessarily identify or target angiogenesis associated with other diseases such as, atherosclerosis, macular degeneration, and rheumatoid arthritis. Recently, our research group developed and characterized a novel murine angiogenesis model, which was not dependent on tumour angiogenesis [21]. This model had readily identifiable and accessible areas of angiogenesis, and showed great potential for non-invasive assessment of particle efficiency.

Several points are worth noticing regarding the MRI analysis. First, the images obtained before and after particle injection have been closely co-localized so that we are looking at almost the exact same spot of the implant. This ensures that the increase seen in the implants is due to particle accumulation and not tissue-differences between before and after images. Secondly, the colour coding of the implants can be closely correlated to the amount of cell infiltration and vascularisation within each implant [21]. This means that voxels with  $R_2$  and  $R_2^*$  values close to zero do not contain cells but only water or other fluids, whereas areas with voxel-values above threshold ( $R_2 < 25 \text{ s}^{-1}$  and  $R_2^* < 95 \text{ s}^{-1}$ . See Figure 1) contain both cells and vasculature.

In our analysis of the MRI data we found statistically significant differences in the  $R_2^*$  relaxation rates, but no significant differences in the  $R_2$  relaxation rates. Although changes in the parameters  $R_1$ ,  $R_2$  and  $R_2^*$  are induced by the iron oxide particles, we would expect the effects to be more distinct in the  $R_2^*$  images. This is due to the sensitivity of  $R_2^*$  towards larger-scale field inhomogeneities created by the iron oxide core of the particles. The increase of mean  $R_2$  and  $R_2^*$  values was converted to percent increase, and a statistically significant difference between the saline group and the two particle groups was observed when looking at the  $R_2^*$  values. Most studies show increased accumulation of targeted versus non-targeted particles [35], which we would have expected to see when comparing the targeted Azure A with the non-targeted Ferumoxtran-10 particle. However, as targeted particles primarily affects the uptake and internalization in cells as well as the speed of accumulation [36, 37, 38], we might have waited too long before imaging the implants after injection of the particles. If we had scanned the mice 2 hours after particle injection, we might have seen a difference between the two groups. From the obtained results we have showed that iron oxide particles do accumulate in the angiogenesis model 24 hours after injection, which is probably attributed to the enhanced permeability and retention effect (EPR-effect) [5, 6, 39].

In conclusion, we assessed hydrodynamic size, zeta potential, and blood circulation half-life of a novel Azure A-conjugated iron oxide particle, and found its biological and physicochemical properties to resemble that of the well described Ferumoxtran-10. Both of these particles were evaluated alongside saline injections in our novel angiogenesis murine model, and both showed localization to areas of angiogenesis. However, in this particular setup we found no distinction between the two particles indicating that the observed accumulation relies primarily on the EPR-effect. Whether another setup would allow the angiogenesis model to distinguish particles from each other remains to be settled, as does the targeting ability of the Azure A particle.

## Acknowledgments

The authors would like to thank Michael Pedersen for providing the Ferumoxtran-10 particles used in the study, Inger Marie Horsman, Dorthe Grand, and Pia Schjerbeck for help and guidance with the animal experiments, and Marianne Verner Bjerre and Marianne Kristiansen for attending to the animals after surgery.

### GRANT SUPPORT

The Danish Programme Commission on Strategic Growth Technologies (NaBIIT, Grant no. 2106-05-0031); The Danish National Research Foundation; The Danish Heart Foundation (Grant no. 08-4-R64-A2037-B953-22462); The Lundbeck Foundation Center for Interventional Research in Radiation Oncology (CIRRO) and The Danish Council for Strategic Research; The Danish Cancer Society (Grant no. DP07002); National Institutes of Health (Grant no. 1R01EB012874-01). Funding sources had no involvement in study design, data collection, or analysis of results.

## REFERENCES

1. Moreno PR, Purushothaman KR, Sirol M, Levy AP, Fuster V. Neovascularization in human atherosclerosis. *Circulation*. 2006; 113:2245–2252. [PubMed: 16684874]
2. Carmeliet P, Jain RK. Angiogenesis in cancer and other diseases. *Nature*. 2000; 407:249–257. [PubMed: 11001068]
3. Kolodgie FD, Narula J, Yuan C, Burke AP, Finn AV, Virmani R. Elimination of neoangiogenesis for plaque stabilization: is there a role for local drug therapy? *J Am Coll Cardiol*. 2007; 49:2093–2101. [PubMed: 17531658]
4. Bergers G, Benjamin LE. Tumorigenesis and the angiogenic switch. *Nat Rev Cancer*. 2003; 3:401–410. [PubMed: 12778130]
5. Iyer AK, Khaled G, Fang J, Maeda H. Exploiting the enhanced permeability and retention effect for tumor targeting. *Drug Discov Today*. 2006; 11:812–818. [PubMed: 16935749]
6. Greish K. Enhanced permeability and retention of macromolecular drugs in solid tumors: a royal gate for targeted anticancer nanomedicines. *J Drug Target*. 2007; 15:457–464. [PubMed: 17671892]
7. Larsen EKV, Nielsen T, Wittenborn T, Birkedal H, Vorup-Jensen T, Jakobsen MH, Ostergaard L, Horsman MR, Besenbacher F, Howard KA, Kjems J. Size-Dependent Accumulation of PEGylated Silane-Coated Magnetic Iron Oxide Nanoparticles in Murine Tumors. *ACS Nano*. 2009; 3:1947–1951. [PubMed: 19572620]
8. Iozzo RV. Matrix proteoglycans: from molecular design to cellular function. *Annu Rev Biochem*. 1998; 67:609–652. [PubMed: 9759499]
9. Larsen EK, Nielsen T, Wittenborn T, Rydtoft LM, Lokanathan AR, Hansen L, Ostergaard L, Kingshott P, Howard KA, Besenbacher F, Nielsen NC, Kjems J. Accumulation of magnetic iron oxide nanoparticles coated with variably sized polyethylene glycol in murine tumors. *Nanoscale*. 2012; 4:2352–2361. [PubMed: 22395568]
10. Corot C, Robert P, Idee JM, Port M. Recent advances in iron oxide nanocrystal technology for medical imaging. *Adv Drug Deliv Rev*. 2006; 58:1471–1504. [PubMed: 17116343]
11. Cormode DP, Skajaa T, Fayad ZA, Mulder WJ. Nanotechnology in medical imaging: probe design and applications. *Arterioscler Thromb Vasc Biol*. 2009; 29:992–1000. [PubMed: 19057023]
12. McCarthy JR, Kelly KA, Sun EY, Weissleder R. Targeted delivery of multifunctional magnetic nanoparticles. *Nanomedicine (Lond)*. 2007; 2:153–167. [PubMed: 17716118]
13. Kessinger CW, Khemtong C, Togao O, Takahashi M, Sumer BD, Gao J. In vivo angiogenesis imaging of solid tumors by alpha(v)beta(3)-targeted, dual-modality micellar nanoprobe. *Exp Biol Med (Maywood)*. 2010; 235:957–965. [PubMed: 20660096]
14. Canet-Soulas E, Letourneur D. Biomarkers of atherosclerosis and the potential of MRI for the diagnosis of vulnerable plaque. *MAGMA*. 2007; 20:129–142. [PubMed: 17605060]
15. Cormode DP, Frias JC, Ma Y, Chen W, Skajaa T, Briley-Saebo K, Barazza A, Williams KJ, Mulder WJ, Fayad ZA, Fisher EA. HDL as a contrast agent for medical imaging. *Clin Lipidol*. 2009; 4:493–500. [PubMed: 20352038]
16. Kramer H, Windrum GM. The metachromatic staining reaction. *J Histochem Cytochem*. 1955; 3:227–237. [PubMed: 14381610]

17. Horobin RW. How Romanowsky stains work and why they remain valuable - including a proposed universal Romanowsky staining mechanism and a rational troubleshooting scheme. *Biotech Histochem.* 2011; 86:36–51. [PubMed: 21235292]
18. Williams WJ, Larson E, Phillips TL. A neoplastic connective tissue mast cell capable of continuous growth in tissue culture. *J Biophys Biochem Cytol.* 1959; 6:361–368. [PubMed: 13844943]
19. Hunziker EB, Ludi A, Herrmann W. Preservation of cartilage matrix proteoglycans using cationic dyes chemically related to ruthenium hexaammine trichloride. *J Histochem Cytochem.* 1992; 40:909–917. [PubMed: 1376743]
20. Szirmai JA. Quantitative Approaches in Histochemistry of Mucopolysaccharides. *Journal of Histochemistry & Cytochemistry.* 1963; 11:24-&.
21. Wittenborn T, Nielsen T, Nygaard JV, Larsen EK, Thim T, Rydtoft LM, Vorup-Jensen T, Kjems J, Nielsen NC, Horsman MR, Falk E. Ultrahigh-field DCE-MRI of angiogenesis in a novel angiogenesis mouse model. *J Magn Reson Imaging.* 2012; 35:703–710. [PubMed: 22031493]
22. Brix H, Lyngby JE, Schierup H-H. Eelgrass (*Zostera marina* L.) as an indicator organism of trace metals in the Limfjord, Denmark. *Mar Environ Res.* 1983; 8:165–181.
23. Andersen MO, Nygaard JV, Burns JS, Raarup MK, Nyengaard JR, Bungler C, Besenbacher F, Howard KA, Kassem M, Kjems J. siRNA nanoparticle functionalization of nanostructured scaffolds enables controlled multilineage differentiation of stem cells. *Mol Ther.* 2010; 18:2018–2027. [PubMed: 20808289]
24. Casula MF, Floris P, Innocenti C, Lascialfari A, Marinone M, Corti M, Sperling RA, Parak WJ, Sangregorio C. Magnetic Resonance Imaging Contrast Agents Based on Iron Oxide Superparamagnetic Ferrofluids. *Chemistry of Materials.* 2010; 22:1739–1748.
25. Owens DE 3rd, Peppas NA. Opsonization, biodistribution, and pharmacokinetics of polymeric nanoparticles. *Int J Pharm.* 2006; 307:93–102. [PubMed: 16303268]
26. Roser M, Fischer D, Kissel T. Surface-modified biodegradable albumin nano- and microspheres. II: effect of surface charges on in vitro phagocytosis and biodistribution in rats. *Eur J Pharm Biopharm.* 1998; 46:255–263. [PubMed: 9885296]
27. Gaumet M, Vargas A, Gurny R, Delie F. Nanoparticles for drug delivery: the need for precision in reporting particle size parameters. *Eur J Pharm Biopharm.* 2008; 69:1–9. [PubMed: 17826969]
28. Gref R, Luck M, Quellec P, Marchand M, Dellacherie E, Harnisch S, Blunk T, Muller RH. 'Stealth' corona-core nanoparticles surface modified by polyethylene glycol (PEG): influences of the corona (PEG chain length and surface density) and of the core composition on phagocytic uptake and plasma protein adsorption. *Colloids Surf B Biointerfaces.* 2000; 18:301–313. [PubMed: 10915952]
29. Mulder WJ, Strijkers GJ, Nicolay K, Griffioen AW. Quantum dots for multimodal molecular imaging of angiogenesis. *Angiogenesis.* 2010; 13:131–134. [PubMed: 20552267]
30. Strijkers GJ, Kluza E, Van Tilborg GA, van der Schaft DW, Griffioen AW, Mulder WJ, Nicolay K. Paramagnetic and fluorescent liposomes for target-specific imaging and therapy of tumor angiogenesis. *Angiogenesis.* 2010; 13:161–173. [PubMed: 20390447]
31. Ellegala DB, Leong-Poi H, Carpenter JE, Klivanov AL, Kaul S, Shaffrey ME, Sklenar J, Lindner JR. Imaging tumor angiogenesis with contrast ultrasound and microbubbles targeted to alpha(v)beta3. *Circulation.* 2003; 108:336–341. [PubMed: 12835208]
32. Leong-Poi H, Christiansen J, Klivanov AL, Kaul S, Lindner JR. Noninvasive assessment of angiogenesis by ultrasound and microbubbles targeted to alpha(v)-integrins. *Circulation.* 2003; 107:455–460. [PubMed: 12551871]
33. Cai W, Chen X. Multimodality molecular imaging of tumor angiogenesis. *J Nucl Med.* 2008; 49(Suppl 2):113S–128S. [PubMed: 18523069]
34. Haubner R, Beer AJ, Wang H, Chen X. Positron emission tomography tracers for imaging angiogenesis. *Eur J Nucl Med Mol Imaging.* 2010; 37(Suppl 1):S86–S103. [PubMed: 20559632]
35. Wang AZ, Gu F, Zhang L, Chan JM, Radovic-Moreno A, Shaikh MR, Farokhzad OC. Biofunctionalized targeted nanoparticles for therapeutic applications. *Expert Opin Biol Ther.* 2008; 8:1063–1070. [PubMed: 18613759]



36. Kirpotin DB, Drummond DC, Shao Y, Shalaby MR, Hong K, Nielsen UB, Marks JD, Benz CC, Park JW. Antibody targeting of long-circulating lipidic nanoparticles does not increase tumor localization but does increase internalization in animal models. *Cancer Res.* 2006; 66:6732–6740. [PubMed: 16818648]
37. Pirollo KF, Chang EH. Does a targeting ligand influence nanoparticle tumor localization or uptake? *Trends Biotechnol.* 2008; 26:552–558. [PubMed: 18722682]
38. Kamaly N, Kalber T, Thanou M, Bell JD, Miller AD. Folate receptor targeted bimodal liposomes for tumor magnetic resonance imaging. *Bioconjug Chem.* 2009; 20:648–655. [PubMed: 19368341]
39. Matsumura Y, Maeda H. A new concept for macromolecular therapeutics in cancer chemotherapy: mechanism of tumoritropic accumulation of proteins and the antitumor agent smancs. *Cancer Res.* 1986; 46:6387–6392. [PubMed: 2946403]

### Highlights

- Synthesis of a potential angiogenesis-targeted nanoparticle.
- Assessment of physicochemical and biological properties.
- Non-invasive evaluation of accumulation in a novel murine angiogenesis model.
- Comparison of synthesized nanoparticle to non-targeted nanoparticle.
- Passive accumulation of both nanoparticles was observed in the angiogenesis model.

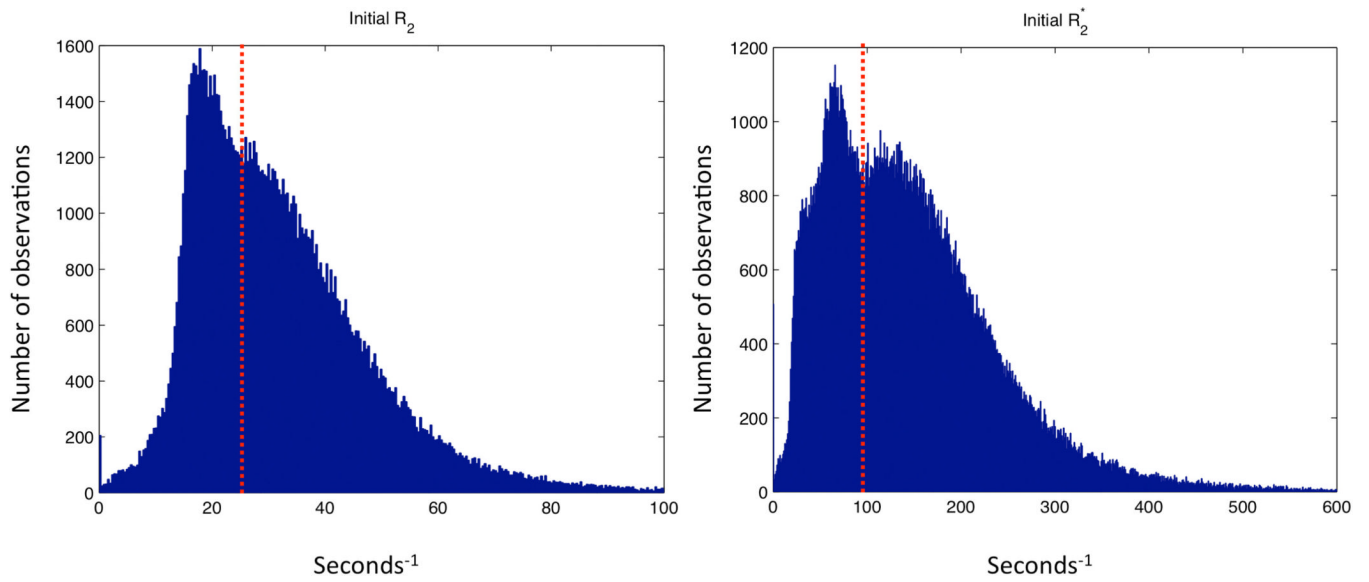


**Figure 1. Bimodal histograms of pooled voxel values**

Voxel values from Regions of Interest from all mice in all groups were pooled into  $R_2$  and  $R_2^*$  histograms enabling the determination of threshold values for tissue-specific areas within the implants.

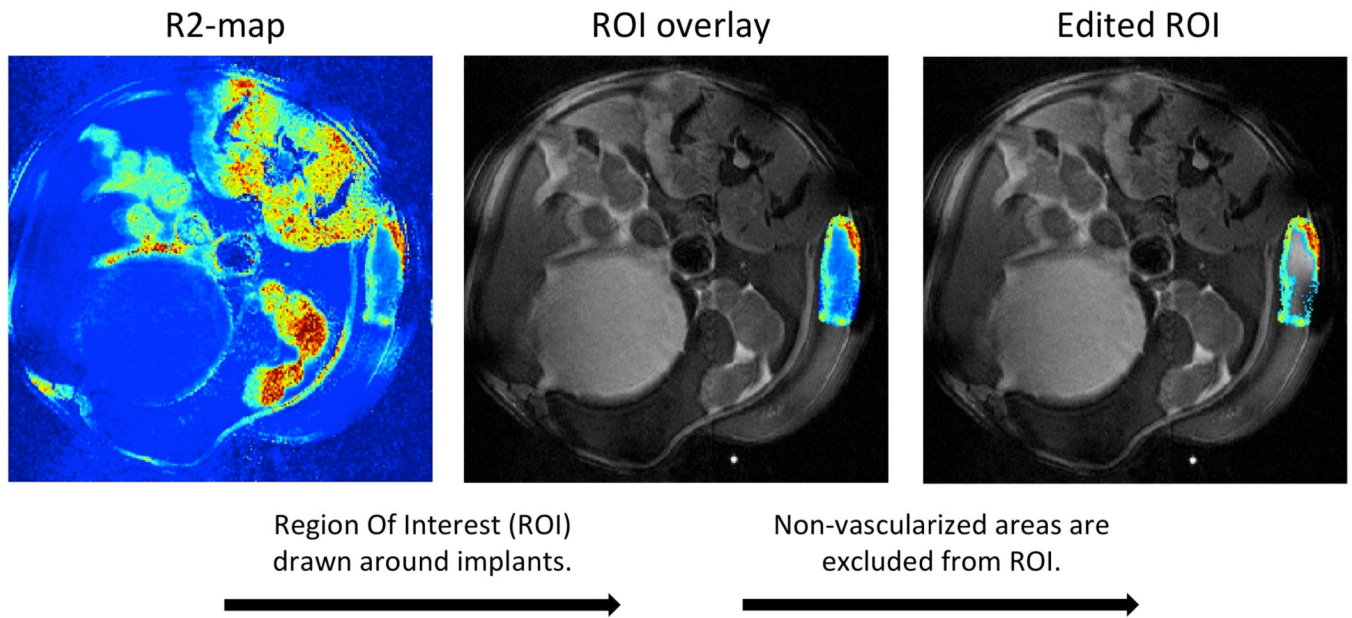


**Figure 2. Image processing from  $R_2$  map to region of interest containing only the cellularized/vascularised implant**

Regions of interest encircling the implanted scaffolds were excised from  $R_2$  maps and overlaid on top of a raw image of the same mouse.  $R_2$ -values below a set threshold value were excluded leaving the cellularized/vascularised area of the implant for further analysis. Procedure was the same for  $R_2^*$  maps.

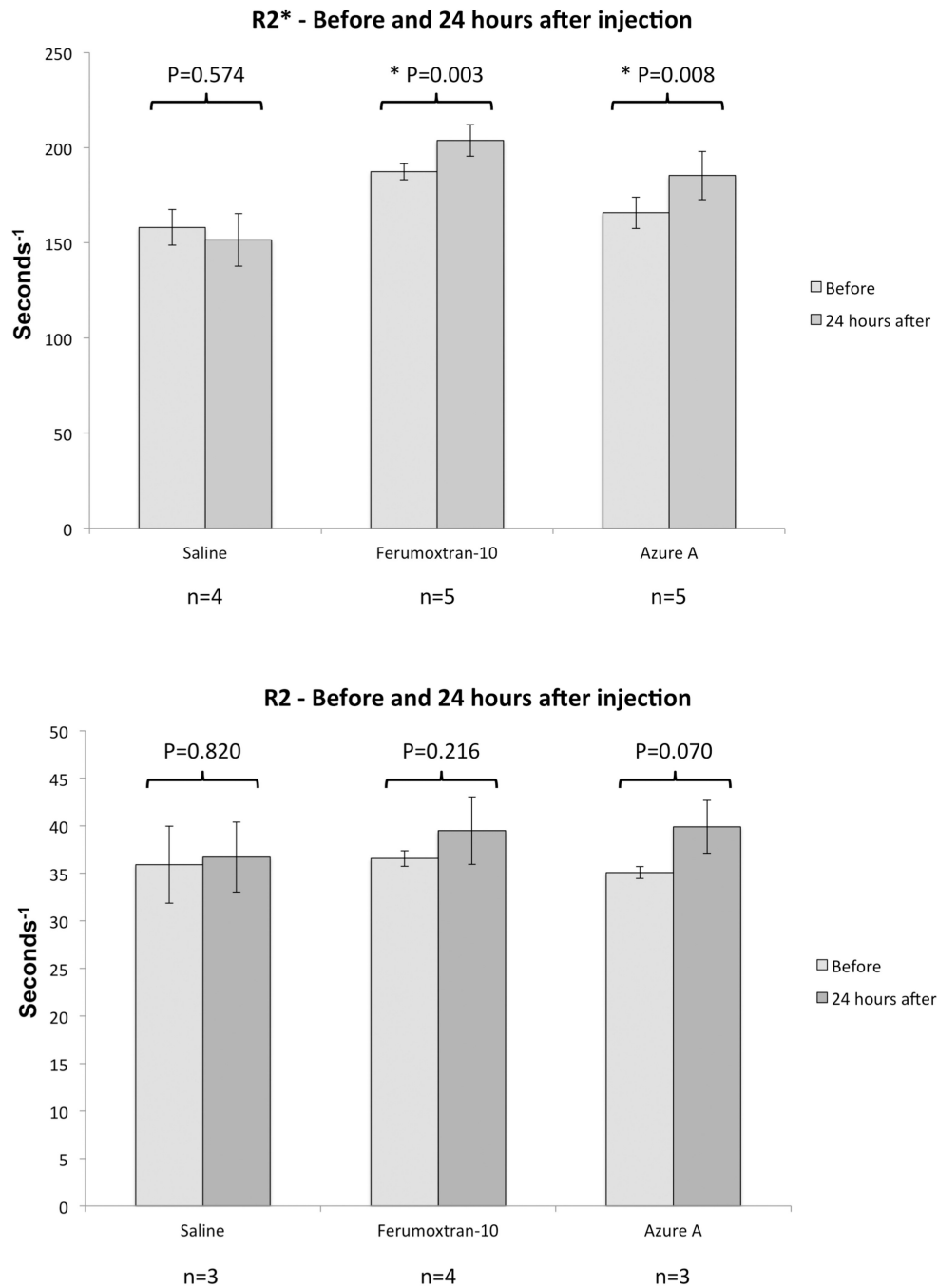


**Figure 3. Mean  $R_2$  and  $R_2^*$  relaxation rates obtained before and after injection of iron oxide particles or saline**

Error bars indicate standard deviation. Asterisks (\*) indicate a statistically significant difference ( $P < 0.05$ ) between the pre-treatment and 24-hour values.

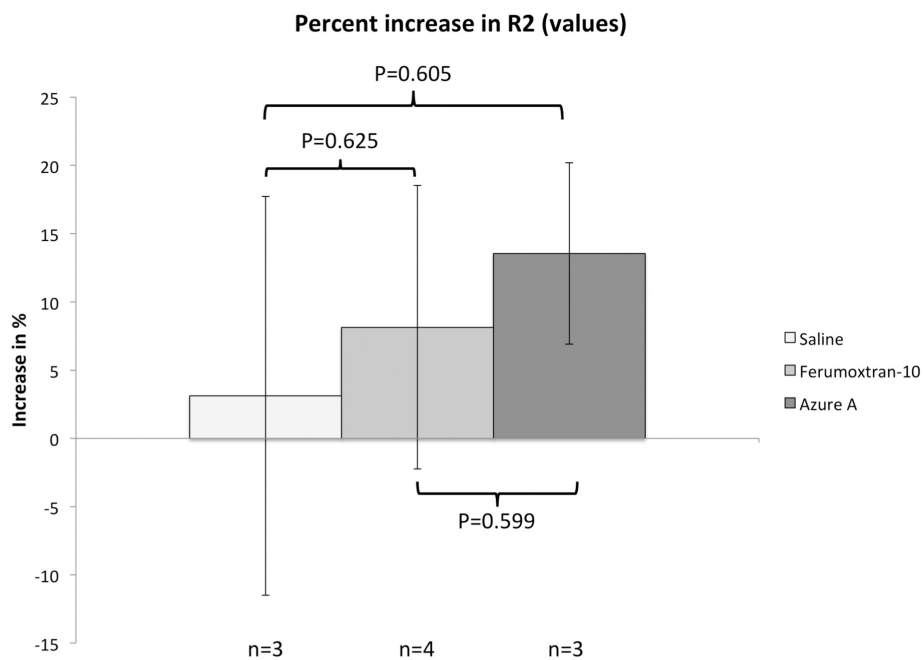
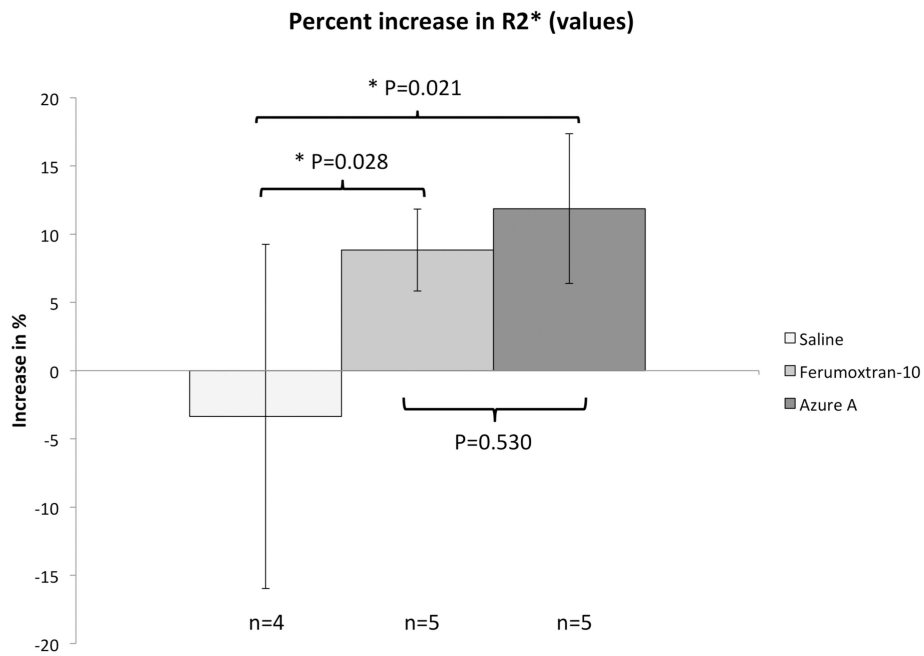


**Figure 4. Relative increase of R<sub>2</sub> and R<sub>2</sub>\* for the three groups**  
 Relative increase in R<sub>2</sub> and R<sub>2</sub>\* relaxation rates were calculated. Error bars indicate standard deviation. Asterisks (\*) indicate a statistically significant difference (P<0.05) between groups.